

Hyperspectral Remote Sensing Image Subpixel Target Detection Based on Supervised Metric Learning

Lefei Zhang, *Member, IEEE*, Liangpei Zhang, *Senior Member, IEEE*, Dacheng Tao, *Senior Member, IEEE*, Xin Huang, *Member, IEEE*, and Bo Du, *Member, IEEE*

Abstract—The detection and identification of target pixels such as certain minerals and man-made objects from hyperspectral remote sensing images is of great interest for both civilian and military applications. However, due to the restriction in the spatial resolution of most airborne or satellite hyperspectral sensors, the targets often appear as subpixels in the hyperspectral image (HSI). The observed spectral feature of the desired target pixel (positive sample) is therefore a mixed signature of the reference target spectrum and the background pixels spectra (negative samples), which belong to various land cover classes. In this paper, we propose a novel supervised metric learning (SML) algorithm, which can effectively learn a distance metric for hyperspectral target detection, by which target pixels are easily detected in positive space while the background pixels are pushed into negative space as far as possible. The proposed SML algorithm first maximizes the distance between the positive and negative samples by an objective function of the supervised distance maximization. Then, by considering the variety of the background spectral features, we put a similarity propagation constraint into the SML to simultaneously link the target pixels with positive samples, as well as the background pixels with negative samples, which helps to reject false alarms in the target detection. Finally, a manifold smoothness regularization is imposed on the positive samples to preserve their local geometry in the obtained metric. Based on the public data sets of mineral detection in an Airborne Visible/Infrared Imaging Spectrometer image and fabric and vehicle detection in a Hyperspectral Mapper image, quantitative comparisons of several HSI target detection methods, as well as some state-of-the-art metric learning algorithms, were performed. All the experimental results demonstrate the effectiveness of the proposed SML algorithm for hyperspectral target detection.

Index Terms—Dimension reduction, hyperspectral image (HSI), metric learning, target detection.

Manuscript received December 19, 2012; revised May 21, 2013 and August 23, 2013; accepted October 10, 2013. This work was supported in part by the National Basic Research Program of China (973 Program) under Grant 2011CB707105 and Grant 2012CB719905; by the Program for Changjiang Scholars and Innovative Research Team in University (IRT1278); by the National Natural Science Foundation of China under Grant 41101336, Grant 61102128, and Grant 41061130553; and by the Program for New Century Excellent Talents in University of China under Grant NCET-11-0396.

L. Zhang and B. Du are with the Computer School, Wuhan University, Wuhan 430072, China (e-mail: zhangleifei@whu.edu.cn; gunspace@163.com).

L. Zhang and X. Huang are with the State Key Laboratory of Information Engineering in Surveying, Mapping, and Remote Sensing, Wuhan University, Wuhan 430079, China (e-mail: zlp62@whu.edu.cn; huang_whu@163.com).

D. Tao is with the Centre for Quantum Computation and Intelligent Systems and the Faculty of Engineering and Information Technology, University of Technology, Sydney, Ultimo, NSW 2007, Australia (e-mail: dacheng.tao@uts.edu.au).

Color versions of one or more of the figures in this paper are available online at <http://ieeexplore.ieee.org>.

Digital Object Identifier 10.1109/TGRS.2013.2286195

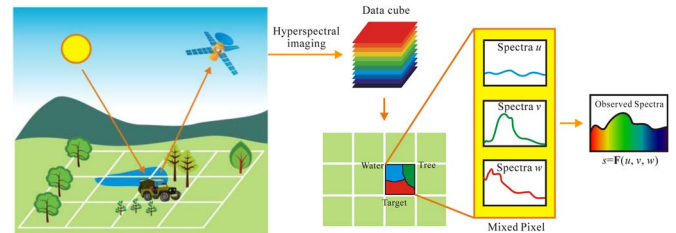


Fig. 1. Illustration of a subpixel target in a mixed pixel of the HSI.

I. INTRODUCTION

HYPERSPECTRAL remote sensing [1] has opened up new opportunities for analyzing a variety of land cover materials due to the rich dimensionality on the spectral domain of each pixel in the hyperspectral image (HSI). Specifically, hyperspectral remote sensing images, such as the images gathered by the Airborne Visible/Infrared Imaging Spectrometer (AVIRIS) [2] spaceborne sensor and the Hyperspectral Mapper (HyMap) [3] airborne sensor, are composed of hundreds of individual and separate but spatially coregistered gray-level images, each of which is captured in a contiguous channel wavelength, with a very high spectral resolution of approximately 10 nm. As a consequence, an HSI is usually regarded as cube data because it has two spatial dimensions (width and height) and a spectral dimension. Since hyperspectral remote sensing can simultaneously provide image data, which contain both spatial and spectral information, one of the most important tasks for HSI applications is to distinguish the few target pixels, such as certain minerals and man-made objects, from the background pixels in the HSI [4]. The basic idea for this detection stems from the fact that the amount of reflectance that varies with the wavelength is unique for any given material if it has been sufficiently characterized. In other words, a target has its representative spectral feature, which can be described as an l -dimensional feature vector, where l is the number of spectral channels of the hyperspectral sensor. Although this spectral feature provides sufficient discriminative information, hyperspectral target detection is always a great challenge because the targets often appear as subpixels in the HSI due to the restriction in the spatial resolution of most hyperspectral sensors [5], [6]. Therefore, depending on the real land cover classes within each pixel, a target pixel in the HSI usually appears as a mixed pixel, which contains both the target material and multiple background classes, as illustrated in Fig. 1.

To deal with mixed pixels in HSI analysis, it is widely accepted that the measured spectrum of a mixed pixel is a function of the pure spectral features (end-members) of all the materials in this pixel, with their weighting factors. The standard technique is the linear mixture model (LMM) [7], which suggests that the measured spectrum is a linear combination of the end-members, weighted by their corresponding abundance fractions, which indicate the proportion of each end-member present in the mixed pixel. The LMM is easy to implement and flexible in most conditions. However, as reviewed in [8], the nonlinear mixture model (NLMM) describes a mixed spectrum by considering some more complex combinations of the component reflectance spectra in the mixture, and often has a physical meaning in that the radiation is reflected by multiple bounces in the hyperspectral imaging. For a more comprehensive explanation of the distinctions between the LMM and the NLMM for HSI spectral unmixing, refer to [9] and [10].

The existing HSI subpixel target detection algorithms in the remote sensing area mainly focus on formulating specific observation models for the target and background pixels [11].

- 1) Spectral-unmixing-based models (structured background models), most of which are LMM based. These methods adopt the LMM with various constraints to characterize the targets and the interfering background, with the consideration of additional random Gaussian sensor noise in the model [12]. The adaptive matched subspace detector (AMSD) is such an algorithm that models the target and background characteristics by the LMM and recognizes the probable subpixel targets by a statistical hypothesis test [13]. It should be noted that the LMM has to be extended into the NLMM in some situations, such as when the source radiation is multiple reflected before being collected at the sensor.
- 2) Statistical-based models (unstructured background models), such as the adaptive matched filter (AMF) [14], [15] and the adaptive coherence/cosine estimator [16], [17]. These models assume that the background samples have specific distributions and maximize the target feature response while suppressing the response of the unknown background feature.
- 3) Hybrid subpixel target detection methods, which formulate the background with both structured and unstructured models. These methods take advantage of the two kinds of model and generally show better performances, particularly when dealing with weak targets in complex backgrounds [18], [19].

However, as aforementioned, all these algorithms follow certain assumptions, and they can only work well in certain conditions, e.g., the AMSD is based on the LMM, and the AMF assumes that the target and background covariance matrices are identical.

In recent years, machine learning algorithms have been introduced into HSI processing, and it has been suggested that they can perform well in the applications of dimension reduction [20], [21], image segmentation [22], [23], and classification [24], [25]. There have been also some related works on HSI target detection [26], e.g., kernel-based target detection methods [27], [28] and sparse-representation-based target detection

methods [29], [30]. However, few studies have been devoted to a target detection method that is benefited by a distance metric in the feature space of HSI, by which target pixels are easily detected in positive space while background pixels are pushed into negative space as far as possible. In fact, based on the key innovative idea of metric learning [31], many different algorithms have been proposed and have been demonstrated to be effective in dealing with challenging applications in computer vision and pattern recognition, e.g., face recognition [32], handwritten digit recognition [33], image retrieval [34], object tracking [35], and gene expression data classification [36]. According to the particular challenges in the HSI target detection task, the following issues should be properly addressed when using metric learning for hyperspectral target detection: 1) as the interested target pixels (positive samples) often appear as subpixels in the HSI, the observed target pixels spectra might be similar to the background pixels (negative samples) spectra in the original feature space; and 2) as the target pixels are often very limited in number and the background pixels belong to various land cover classes, which include almost all the pixels in the HSI [37], the learned distance metric should remove as many background pixels as possible from the target pixels.

In this paper, a novel supervised metric learning (SML) algorithm, which can effectively learn a distance metric for HSI target detection, is introduced in response to the aforementioned two aspects. As a machine-learning-based approach, no physically meaningful model is needed. By considering the spectral features of both negative samples (background pixels) and positive samples (mixed pixels with the target signature), the distance metric provided by SML results in the target pixels being easily detected in positive space while the background pixels are pushed into negative space as far as possible. Thus, the target detection measurement can be obtained by the spectral similarity between the test sample and the prior target feature using the learned distance metric. In particular, the SML algorithm first maximizes the distance between the positive and negative samples by a supervised distance maximization. Then, by considering that the background pixels belong to various classes, a similarity propagation constraint is added into the SML to simultaneously link the target pixels with positive samples, as well as the background pixels with negative samples, which helps to reduce the false alarm rate. Finally, a manifold smoothness regularization of all the positive samples is considered to preserve their local geometry in the obtained metric.

The rest of this paper is organized as follows. In Section II, we give a brief review of the metric learning algorithms. We then provide the detailed explanation of our SML algorithm for HSI subpixel target detection in Section III. The HSI target detection experimental results are reported in Section IV, followed by the conclusion in Section V.

II. RELATED WORKS

We assume that we have the following given data set $\mathbf{X} = [\mathbf{x}_1, \dots, \mathbf{x}_n] \in R^{l \times n}$, in which n is the number of samples and l is the number of features, with the label information $\mathbf{C} =$

$[c_1, \dots, c_n]^T$, $c_i \in \{+1, -1\}$. Thus, we have the following similar constraints set Λ and dissimilar constraints set Ω :

$$\Lambda : \forall (\mathbf{x}_i, \mathbf{x}_j) |_{c_i=c_j} \in \Lambda \quad (1)$$

$$\Omega : \forall (\mathbf{x}_i, \mathbf{x}_j) |_{c_i \neq c_j} \in \Omega. \quad (2)$$

The goal of metric learning is to learn a Mahalanobis-like distance metric $d(\mathbf{x}_i, \mathbf{x}_j)$, by which the distance between \mathbf{x}_i and \mathbf{x}_j can be computed as

$$d(\mathbf{x}_i, \mathbf{x}_j) = \sqrt{(\mathbf{x}_i - \mathbf{x}_j)^T \mathbf{M} (\mathbf{x}_i - \mathbf{x}_j)}. \quad (3)$$

To ensure that $d(\mathbf{x}_i, \mathbf{x}_j)$ is a metric, the learned Mahalanobis-like matrix $\mathbf{M} \in \mathbb{R}^{l \times l}$ must be symmetric and positive semidefinite. Note that if $\mathbf{M} = \mathbf{I}$, then the Mahalanobis-like distance is equal to the Euclidean distance. If \mathbf{M} is restricted to be diagonal, then the distance metric is equal to the Euclidean distance, but the different features are given different weights. Furthermore, we can find a nonsquare matrix $\mathbf{W} \in \mathbb{R}^{l \times d}$ ($d \leq l$) to jointly perform dimensionality reduction (DR) and metric learning [38], [39]

$$\begin{aligned} d(\mathbf{x}_i, \mathbf{x}_j) &= \sqrt{(\mathbf{x}_i - \mathbf{x}_j)^T \mathbf{M} (\mathbf{x}_i - \mathbf{x}_j)} \\ &= \sqrt{(\mathbf{x}_i - \mathbf{x}_j)^T \mathbf{W} \mathbf{W}^T (\mathbf{x}_i - \mathbf{x}_j)} \\ &= \| \mathbf{W}^T \mathbf{x}_i - \mathbf{W}^T \mathbf{x}_j \|. \end{aligned} \quad (4)$$

Learning such a distance metric \mathbf{M} as given in (4) is equivalent to finding a DR transformation of data that replaces each point $\mathbf{x}_i \in \mathbb{R}^l$ with $\mathbf{W}^T \mathbf{x}_i \in \mathbb{R}^d$ and applying the standard Euclidean distance to the new data [31].

The various different distance metric learning methods usually learn a specific matrix \mathbf{M} (or \mathbf{W}) under the supervision of constraint sets Λ and Ω , such that the samples from different classes can be well discriminated. Xing *et al.* [31] formulated such a problem as a constrained convex programming algorithm, and the method introduced by Davis *et al.* [40] learns the Mahalanobis distance function from an information-theoretic perspective. Relevant component analysis (RCA) [41] uses adjustment learning to reduce irrelevant variability in the data while amplifying relevant variability. Discriminative component analysis (DCA) [34] extends RCA by the exploitation of negative constraints and captures the nonlinear relationships between data instances with the contextual information. Large margin nearest neighbor (LMNN) [33] trains the metric with the goal that the k -nearest neighbors (KNNs) always belong to the same class while examples from different classes are separated by a large margin. Neighborhood component analysis (NCA) [32] learns the distance metric by maximizing a stochastic variant of the leave-one-out KNNs score on the training set.

III. SML ALGORITHM FOR HSI TARGET DETECTION

Fig. 2 shows the flowchart of the SML algorithm for HSI target detection. The input items of SML include a set of positive samples (red points) and negative samples (green points). The SML algorithm is then performed, the full optimization of

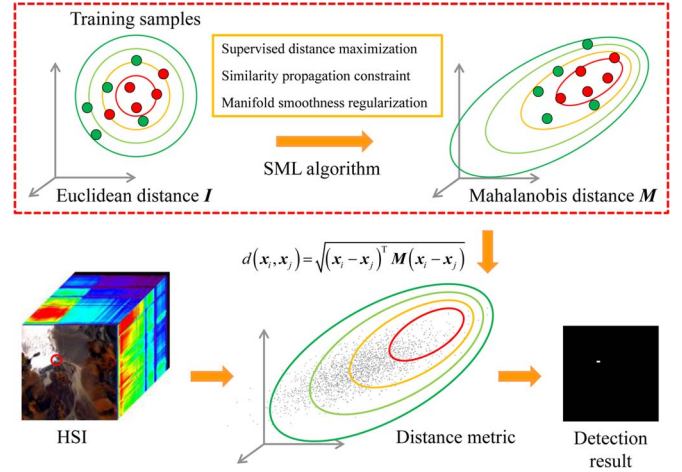


Fig. 2. Flowchart of the SML algorithm for HSI target detection.

which consists of the following three parts: 1) a supervised distance maximization; 2) a similarity propagation constraint; and 3) a manifold smoothness regularization. Detailed explanations of these three parts are given in the following discussion. Since the SML learned distance metric is technically designed to be beneficial for HSI target detection, the target detection task is then simply achieved by sorting the samples that are nearest neighbors of the prior target feature, using the Mahalanobis-like distance metric in (4).

A. Supervised Distance Maximization

We follow the definitions given in the previous section in that we have the observed data set $\mathbf{X} \in \mathbb{R}^{l \times n}$ with its label information $\mathbf{C} \in \mathbb{R}^n$. Here, n is the number of training samples, and l is the number of spectral channels in the HSI. We further denote n^+ and n^- as the number of positive and negative samples, respectively; and thus, $n = n^+ + n^-$. Similar to [35] and [42], supervised distance maximization for target detection is measured by maximizing the average distance between positive and negative samples while minimizing the average distance between positive samples in the learned distance metric. By unifying the preceding two aspects together, we have

$$\arg \max_{\mathbf{W}} \left(\frac{\sum_i^{c_i=+1} \sum_j^{c_j=-1} \| \mathbf{W}^T \mathbf{x}_i - \mathbf{W}^T \mathbf{x}_j \|^2}{n^+ n^-} - \alpha \frac{\sum_i^{c_i=+1} \sum_j^{c_j=+1} \mathbf{Q}_{ij} \| \mathbf{W}^T \mathbf{x}_i - \mathbf{W}^T \mathbf{x}_j \|^2}{n^+ n^+} \right) \quad (5)$$

in which $\alpha > 0$ is a weighting factor used to control these two parts; the matrix $\mathbf{Q} \in \mathbb{R}^{n^+ \times n^+}$ in (5) is introduced from Laplacian eigenmaps [43] for locality preservation. Thus

$$\mathbf{Q}_{ij} = \exp(\| \mathbf{x}_i - \mathbf{x}_j \|^2 / t) \quad (6)$$

in which the radius parameter t can be experientially set to the sum of the variance of all the positive samples.

The supervised distance maximization in (5) finds a metric distance that is the most discriminative for distinguishing target pixels from background ones. However, it only tries to maximize the average pairwise distances among the positive and negative samples, and there are no restraints on the negative and positive samples to deal with the variety of background spectra and the local geometry of the target manifold space, respectively. We therefore further impose the following similarity propagation constraint and manifold smoothness regularization into the SML.

B. Similarity Propagation Constraint

To enable the proposed SML to work well for HSI target detection, we should give more restraint to each training sample to further shrink the distances between similar pairs. In this paper, a similarity propagation constraint is suggested to simultaneously link the target pixels with positive samples, as well as the background pixels with negative samples. This constraint aims to learn an optimal intrinsic similarity matrix $\mathbf{S} \in \mathbb{R}^{n \times n}$, which measures the similarities between all the sample pairs by propagating a strong similarity (defined by the label information) to all the samples with a weak similarity. A common way to build the weak similarity of sample pairs is the KNN-graph-based pairwise connection, which is defined by the neighborhood indicator matrix $\mathbf{G} \in \mathbb{R}^{n \times n}$, i.e.,

$$\mathbf{G}_{ij} = \begin{cases} 1, & \mathbf{x}_j \in \mathbf{K}(\mathbf{x}_i) \\ 0, & \text{otherwise} \end{cases} \quad (7)$$

in which $\mathbf{G}_{ii} \big|_{i=1}^n = 0$, and $\mathbf{K}(\mathbf{x}_i)$ denotes the sample set of the KNNs of \mathbf{x}_i by the Euclidean metric in the whole set. Note that such a matrix \mathbf{G} holds weak (probably correct) similarities between all the sample pairs since it does not address any supervised information from the training samples. To build a strong similarity matrix $\mathbf{H} \in \mathbb{R}^{n \times n}$, we have

$$\mathbf{H}_{ij} = \begin{cases} 1, & \mathbf{x}_j \in \mathbf{K}(\mathbf{x}_i) |_{(\mathbf{x}_i, \mathbf{x}_j) \in \Lambda} \\ 0, & \text{otherwise} \end{cases} \quad (8)$$

in which $\mathbf{K}(\mathbf{x}_i) |_{(\mathbf{x}_i, \mathbf{x}_j) \in \Lambda}$ finds the KNNs of \mathbf{x}_i , also by the Euclidean metric, but only in the similar constraints set Λ . Again, we have $\mathbf{H}_{ii} \big|_{i=1}^n = 0$ in (8).

For the initialization of the expected matrix \mathbf{S} , we simply set $\mathbf{S}^{(0)} = \mathbf{H}$ and $\mathbf{S}_{ii}^{(0)} \big|_{i=1}^n = 1$. We then regard the elements where $\mathbf{S}_{ij}^{(0)} = 1$ as original positive energies and try to propagate these energies to the other 0 elements in $\mathbf{S}^{(0)}$, following the paths built in the weak similarity matrix \mathbf{G} . The criterion of this similarity propagation can be formulated as [44]

$$\mathbf{S}_i^{(t+1)} = (1 - \gamma)\mathbf{S}_i^{(0)} + \gamma \frac{\sum_j \mathbf{G}_{ij} \mathbf{S}_j^{(t)}}{\sum_j \mathbf{G}_{ij}} \quad (9)$$

where $\mathbf{S}_i^{(t)}$ denotes the i th row of matrix \mathbf{S} at the t th iteration, and γ is a parameter in the similarity propagation restricted by $0 < \gamma < 1$, which indicates the relative amount of the informa-

tion from its neighbors and its initial supervised information. The matrix form of (9) is written as

$$\mathbf{S}^{(t+1)} = (1 - \gamma)\mathbf{S}^{(0)} + \gamma \mathbf{P} \mathbf{S}^{(t)} \quad (10)$$

in which $\mathbf{P} = \mathbf{D}^{-1} \mathbf{G}$, as with the well-known transition probability matrix in the Markov random walk models, and \mathbf{D} is a diagonal matrix whose diagonal elements equal the sum of the corresponding row elements in \mathbf{G} , i.e., $\mathbf{D}_{ii} = \sum_j \mathbf{G}_{ij}$.

Since $0 < \gamma < 1$ and the eigenvalues of \mathbf{P} are in $[-1, 1]$, the sequence $\{\mathbf{S}^{(t)}\}$ converges, and it suffices to solve the limit as [45]

$$\mathbf{S}^* = \lim_{t \rightarrow \infty} \mathbf{S}^{(t)} = (1 - \gamma)(\mathbf{I} - \gamma \mathbf{P})^{-1} \mathbf{S}^0. \quad (11)$$

Thus, we can compute \mathbf{S}^* directly without iterations. It is worth noting that $(\mathbf{I} - \gamma \mathbf{P})^{-1}$ is in fact a graph or a diffusion kernel [46]. Next, we can obtain the expected similarity matrix \mathbf{S} by symmetrizing \mathbf{S}^* and removing the small similarity values, i.e.,

$$\mathbf{S} = \left(\frac{\mathbf{S}^* + \mathbf{S}^{*T}}{2} \right)_{\geq \varphi}. \quad (12)$$

In (12), we zero out the elements of \mathbf{S} , whose absolute values are smaller than the threshold φ .

By the aforementioned similarity matrix \mathbf{S} , we have the similarity propagation constraint

$$\arg \min_{\mathbf{W}} \left(\frac{\sum_i \sum_j \mathbf{S}_{ij} \|\mathbf{W}^T \mathbf{x}_i - \mathbf{W}^T \mathbf{x}_j\|^2}{n^2} \right). \quad (13)$$

Subsequently, by adding (13) into (5) with a weighting factor $\beta > 0$, we have

$$\arg \max_{\mathbf{W}} \left(\frac{\sum_i^{c_i=+1} \sum_j^{c_j=-1} \|\mathbf{W}^T \mathbf{x}_i - \mathbf{W}^T \mathbf{x}_j\|^2}{n^+ n^-} - \alpha \frac{\sum_i^{c_i=+1} \sum_j^{c_j=+1} \mathbf{Q}_{ij} \|\mathbf{W}^T \mathbf{x}_i - \mathbf{W}^T \mathbf{x}_j\|^2}{n^+ n^+} - \beta \frac{\sum_i \sum_j \mathbf{S}_{ij} \|\mathbf{W}^T \mathbf{x}_i - \mathbf{W}^T \mathbf{x}_j\|^2}{n^2} \right). \quad (14)$$

In order to simplify the optimization (14), we build a unified matrix $\mathbf{T} \in \mathbb{R}^{n \times n}$ with the same size as the similarity matrix \mathbf{S} , each element of which encodes a pairwise weighting factor provided in (14). Matrix \mathbf{T} can be easily obtained by considering separately for each part and then putting them together as a whole, i.e.,

$$\mathbf{T}_{ij} = \begin{cases} -\beta \mathbf{S}_{ij} / n^2 - \alpha \mathbf{Q}_{ij} / n^{+2}, & c_i = c_j = +1 \\ -\beta \mathbf{S}_{ij} / n^2, & c_i = c_j = -1 \\ -\beta \mathbf{S}_{ij} / n^2 + 1 / n^+ n^-, & c_i c_j = -1. \end{cases} \quad (15)$$

We then rewrite (14) as

$$\begin{aligned}
& \arg \max_{\mathbf{W}} \left(\sum_i \sum_j \mathbf{T}_{ij} \|\mathbf{W}^T \mathbf{x}_i - \mathbf{W}^T \mathbf{x}_j\|^2 \right) \\
&= \arg \max_{\mathbf{W}} \text{tr} [\mathbf{W}^T \mathbf{X}(\mathbf{R} - \mathbf{T})\mathbf{X}^T \mathbf{W}] \\
&= \arg \max_{\mathbf{W}} \text{tr} (\mathbf{W}^T \mathbf{X} \mathbf{L} \mathbf{X}^T \mathbf{W}) \\
&= \arg \max_{\mathbf{W}} \text{tr} (\mathbf{W}^T \mathbf{E} \mathbf{W}) \tag{16}
\end{aligned}$$

in which \mathbf{R} is a diagonal matrix whose diagonal elements are equal to the sums of the corresponding row elements in \mathbf{T} , i.e., $\mathbf{R}_{ii} = \sum_j \mathbf{T}_{ij}$, and $\mathbf{L} = \mathbf{R} - \mathbf{T}$ is known as the graph Laplacian [43]. In order to further reduce (16), we denote $\mathbf{E} = \mathbf{X} \mathbf{L} \mathbf{X}^T$.

C. Manifold Smoothness Regularization

In the HSI subpixel target detection task, since the target pixels are mixed with the background pixels from various classes, the input positive samples will be usually embedded in a compact subspace, i.e., a low-dimensional manifold, considering the spectral mixture, and thus, we expect the learned manifold of these positive samples to be as smooth as possible. In the proposed SML, the manifold smoothness of all the positive samples is considered as an additional regularization to preserve their local geometry in the obtained metric [47], [48]. The manifold smoothness can be quantitatively measured by the reconstruction error of the famous locally linear embedding (LLE) algorithm [49]. In this work, we use a linear version of LLE to build the minimization of the reconstruction error for the positive samples. Following the aforementioned definitions, we denote the positive sample set as $\mathbf{X}^+ = [\mathbf{x}_1^+, \dots, \mathbf{x}_{n^+}^+] \in \mathbb{R}^{l \times n^+}$. For each positive sample \mathbf{x}_i^+ , the reconstruction error is computed by the linear combination of the other samples $\mathbf{x}_j^+ |_{j \neq i}$ with weight $\mathbf{A}_{ij} |_{j \neq i}$, respectively. Thus

$$\arg \min_{\mathbf{A}_{ij}} \left\| \mathbf{x}_i^+ - \sum_{j \neq i} \mathbf{A}_{ij} \mathbf{x}_j^+ \right\|^2 \tag{17}$$

where $\mathbf{A} \in \mathbb{R}^{n^+ \times n^+}$, and $\mathbf{A}_{ii} = 0$. By the weight matrix given above, we minimize the sum of the reconstruction errors of all the positive samples in the measured space as

$$\arg \min_{\mathbf{W}} \sum_i \left\| \mathbf{W}^T \mathbf{x}_i^+ - \sum_{j \neq i} \mathbf{A}_{ij} \mathbf{W}^T \mathbf{x}_j^+ \right\|^2. \tag{18}$$

We can further rewrite (18) as follows:

$$\begin{aligned}
& \arg \min_{\mathbf{W}} \text{tr} [\mathbf{W}^T \mathbf{X}^+ (\mathbf{I} - \mathbf{A}^T) (\mathbf{I} - \mathbf{A}^T)^T \mathbf{X}^{+T} \mathbf{W}] \\
&= \arg \min_{\mathbf{W}} \text{tr} [\mathbf{W}^T \mathbf{B} \mathbf{W}] \tag{19}
\end{aligned}$$

where $\mathbf{B} = \mathbf{X}^+ (\mathbf{I} - \mathbf{A}^T) (\mathbf{I} - \mathbf{A}^T)^T \mathbf{X}^{+T}$.

Finally, by combining the supervised distance maximization with the similarity propagation constraint introduced in (16)

and the manifold smoothness regularization provided in (19), we have the final optimization of SML, i.e.,

$$\begin{aligned}
& \arg \min_{\mathbf{W}} \text{tr} [\mathbf{W}^T \mathbf{E} \mathbf{W} - \mu (\mathbf{W}^T \mathbf{B} \mathbf{W})] \\
&= \arg \min_{\mathbf{W}} \text{tr} [\mathbf{W}^T (\mathbf{E} - \mu \mathbf{B}) \mathbf{W}] \\
&= \arg \min_{\mathbf{W}} \text{tr} (\mathbf{W}^T \mathbf{Z} \mathbf{W}) \tag{20}
\end{aligned}$$

in which μ is a weighting factor, and $\mathbf{Z} = \mathbf{E} - \mu \mathbf{B}$. Equation (20) is famous in graph embedding methods [50], [51] and is often enforced by a constraint in (21), which helps to remove the arbitrary scaling factor and uniquely determines \mathbf{W} , i.e.,

$$\arg \min_{\mathbf{W}} \text{tr} (\mathbf{W}^T \mathbf{Z} \mathbf{W}) \quad \text{s.t.} \quad \mathbf{W} \mathbf{W}^T = \mathbf{I}. \tag{21}$$

The solution of (21) is given by the top d eigenvectors associated with the d smallest eigenvalues of the standard eigenvalue decomposition

$$\mathbf{Z} \mathbf{v} = r \mathbf{v}. \tag{22}$$

IV. EXPERIMENTS

The experiments for HSI target detection are implemented on two public data sets.

- 1) An AVIRIS image, which covers the lunar crater volcanic field (LCVF) in Northern Nye County, NV, USA. This data set is public and is available at the National Aeronautics and Space Administration website. Considered as a standard data set in HSI analysis, extensive research work has been undertaken in this area [52], [53]. The full spatial size of the LCVF data set is 6955 lines, with 781 samples for each line. In our experiment, we use a subimage with a size of 400×400 pixels, the land cover types of which have been previously investigated and comprise five main land cover classes, namely, red oxidized basaltic cinders, rhyolite, playa (dry lakebed), shade, and vegetation. We then implant the almandine spectrum into the image to simulate the subpixel targets for detection. The spatial resolution of the image is approximately 20 m, and there are 224 spectral channels from 0.4 to 2.5 μm .
- 2) A HyMap image, which was captured at the location of the small town of Cook City, MT, USA, on July 4, 2006. This image is a part of the Target Detection Test project [54] published by the Rochester Institute of Technology (RIT), Rochester, NY, USA, to serve as a standard data set in HSI target detection. This data set project is also equipped with the exact locations and spectral library files (SPL) of all the desired targets. The full image size is 280×800 pixels, with 126 spectral channels in the visible-to-near infrared (VNIR)–short wave infrared (SWIR) range. The ground spatial resolution of the HSI is about 3 m, and the spectral resolution is about 14 nm.

A. AVIRIS Experiment

The LCVF image scene used in our experiment is shown in Fig. 3(a). In this HSI scene, we aim to detect the implanted

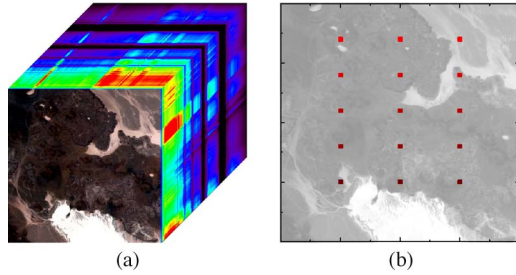


Fig. 3. (a) AVIRIS data cube of the LCVF. (b) Implanted target locations in the AVIRIS image.

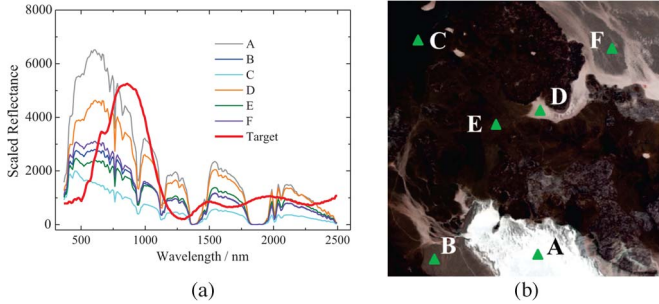


Fig. 4. (a) Implanted pure target spectrum and some representative background samples spectra. (b) Locations of the background samples given in (a).

TABLE I
DETAILS OF THE IMPLANTED TARGET PANELS IN FIG. 3

Color	Line index	Sample index	Fraction
■	60	(100, 101) (200, 201) (300, 301)	10%
■	120	(100, 101) (200, 201) (300, 301)	8%
■	180	(100, 101) (200, 201) (300, 301)	6%
■	240	(100, 101) (200, 201) (300, 301)	4%
■	300	(100, 101) (200, 201) (300, 301)	2%

subpixel targets with different implanted fractions. The target of interest is a mineral spectra named almandine, and we obtained its standard spectrum from the Environment for Visualizing Images spectral library (U.S. Geological Survey). The spectral range of the pure target spectrum is from 0.39510 to 2.56000 μm , with a spectral resolution of 0.002 μm . Therefore, in order to make it consistent with the AVIRIS data cube, we rescale the target spectra to the image range and resample it according to the HSI wavelength. The adopted pure target spectrum and some representative background spectral curves are shown in Fig. 4(a), and the locations of the background pixels are highlighted in Fig. 4(b). Then, in order to simulate a series of subpixels, to make the quantitative analysis possible, 15 target panels are implanted into the image, the locations of which are given in Fig. 3(b).

The added target panels have the same size, i.e., two pixels for each target panel, and the detailed coordinates of all 30 implanted target pixels are given in Table I. Note that all the implanted target pixels are mixed pixels, and each spectrum x is mixed with the prior target spectrum t and the original

background spectra b at the implanted locations, respectively, by both the LMM (23) and a representative NLMM (24), to evaluate the algorithms performance in subpixel target detection. Thus

$$x = pt + (1 - p)b \tag{23}$$

$$x = \sqrt{pt^2 + (1 - p)b^2} \tag{24}$$

in which the implanted fraction p varies from 10% to 2%, as indicated in Table I.

1) *Linear Implanted Target Detection Results:* We now evaluate the subpixel target detection performance of the proposed algorithm. The SML algorithm requires training samples to learn the distance metric; however, in the general hyperspectral target detection task, only the pure target spectrum is available as prior information. Thus, in this paper, we propose to generate the training samples for SML as follows: 1) for the negative samples, we randomly select a certain number of pixels from the HSI to represent the different background land cover classes, and we then set the number of negative samples as [10, 20, 30, 40, 50] to explore its effect on the detection accuracy; and 2) for the positive samples, we mix the aforementioned negative samples with the prior target spectrum, linearly or nonlinearly, by a fixed fraction of $p = 0.1$, to simulate the various subpixel targets as the positive samples for the SML algorithm. Hence, the number of positive samples is equal to the number of negative samples in our experiments. Note that there are five parameters in the SML algorithm, which we should predefine as inputs. To address this issue, we propose to specifically determine their values as follows: We experimentally set parameter α to 1 in the supervised distance maximization term and set parameter γ to 0.9 in the similarity propagation constraint. The radius parameter t is set to the sum of the variance of all the positive samples, as aforementioned. The regularization parameters β and μ are data dependent, and thus, we have to optimize them by twofold cross-validation on the training samples. Empirically, these two parameters are usually chosen as very small values for SML; in our experiments, they are tuned by the range of $\beta, \mu \in 10^{[-6, -5, \dots, -2]}$.

For the linear implanted targets, Fig. 5(a)–(e) shows the receiver operating characteristic (ROC) [55] curves of the proposed algorithm with an increasing number of negative samples from 10 to 50. It is clear that, when the number of negative samples is low, the target detection performance is poor, because the SML algorithm requires more negative samples, which can represent the various background land cover classes in HSI to learn a better distance metric for discrimination. As a result, the ROC curves improve as the number of negative samples increases, as shown in Fig. 5(b) and (c). When the number of negative samples is increased to a larger value, the target detection results achieve a stable performance. Fig. 5(a)–(e) also empirically show the effect of the similarity propagation constraint (13) and the manifold smoothness regularization (19). In these figures, the solid lines indicate the ROC curves of the proposed SML, whereas the dashed lines give the performance of the distance metric learned by supervised distance maximization (SDM), i.e., the optimization suggested in (5). It is shown that the

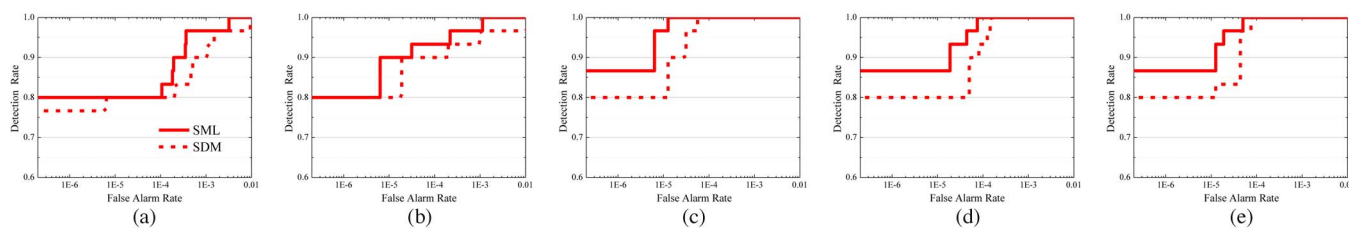


Fig. 5. (a)–(e) ROC curves of the SML and SDM algorithms with increasing numbers of negative samples (from 10 to 50).

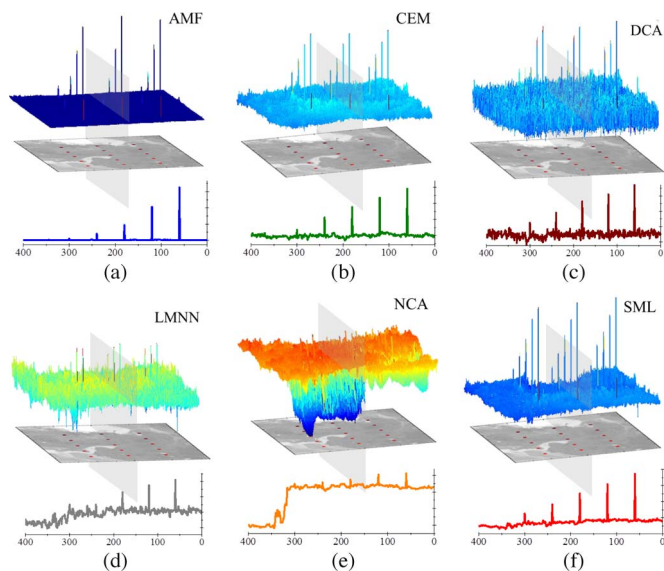


Fig. 6. Three-dimensional target detection test statistic plots and 1-D transect plots of (a) AMF, (b) CEM, (c) DCA, (d) LMNN, (e) NCA, and (f) SML in the linear implanted target experiment.

proposed SML outperforms SDM in all the ROC curves, which confirms the effectiveness of the recommended regularizations.

We then show the target detection results of the proposed SML compared with some of the other state-of-the-art technologies on the AVIRIS data set, also for the linear implanted targets. The AMF [17], constrained energy minimization (CEM) [52], DCA [34], LMNN [33], and NCA [32] algorithms are applied as the comparisons in the experiment. Among these algorithms, AMF and CEM are effective HSI subpixel target detection algorithms that only need the desired target spectrum as input, whereas DCA, LMNN, and NCA are also distance metric learning algorithms that require a set of training samples. Thus, we adopt the same training samples as SML, with the number of negative samples being 30, to learn the Mahalanobis-like distance metric for these four metric learning approaches.

Fig. 6(a)–(f) show the 3-D target detection test statistic plots of all the aforementioned algorithms. For AMF and CEM, we directly show the algorithm output value as the test statistic for each pixel in Fig. 6(a) and (b), whereas for the latter four distance metric learning algorithms, the target detection results are measured by the distance of each pixel spectrum to the prior target spectrum using the learned Mahalanobis-like distance metric. In order to unify the presentation, we show the reciprocal of the distance as the test statistic in Fig. 6(c)–(f). Thus, as shown in Fig. 6, the higher test statistic indicates a higher level of probability that the desired target presents at a certain pixel and vice versa. From these test statistic plots, we

can see that the target locations are obvious in the top three lines of the target panels (implanted fractions are no less than 6%) for all the algorithms; however, when the abundance of the target in a mixed pixel is less than 6%, e.g., the bottom two lines of the target panels, which can be hardly observed in most of the algorithms, the separability between the target and the background pixels is weak. Among these figures, the proposed SML suppresses the background pixels to a slightly lower range, and the target pixels can be easily recognized. It should be emphasized that, although the AMF algorithm can suppress the background pixels to an even lower value, some of the target pixels are not clear enough, and the last line of the target panels (2% implanted fraction), in particular, is totally missed in the detection.

To make the aforementioned target–background separability analysis even clearer, we also show the 1-D transect plots of all the algorithms in Fig. 6(a)–(f). These plots are the transects of sample 200 in the 3-D target detection test statistic plots of all the algorithms, respectively, each of which has five implanted target pixels at the line indices of 60, 120, 180, 240, and 300. As aforementioned, a higher test statistic value indicates a higher level of probability that the desired target presents at a certain pixel. These 1-D transect plots further illustrate that only AMF, CEM, and the proposed SML algorithms can suppress the background pixels to a low and steady range; furthermore, the expected peak in the transect plot of the target pixel at line 300 (2% implanted fraction) can be hardly seen in Fig. 6(a), but can be observed in Fig. 6(f), which suggests that SML can reveal better separability between the target and background pixels.

To obtain the final target detection map, as shown in Fig. 2, threshold-based binary segmentation technology is performed in Fig. 6(a)–(f). Specifically, all the pixels in the 3-D test statistic plot that are higher than a certain threshold are considered as a desired target, whereas the other pixels are rejected as background pixels. As a result, the target detection rate (TRR) and its associated false alarm rate (FAR) are closely related to the chosen threshold. Here, we again use ROC curves to comprehensively evaluate the final detection performances, which are obtained by computing the TRR versus FAR with the varied thresholds, as we reported in Fig. 5(a)–(e). The algorithm with the best performance is indicated by a curve that is nearest to the upper left of the figure, which indicates the highest TRR under the same FAR. Fig. 7(a) shows the target detection ROC curves of all the reference algorithms in the linear implanted target experiment. These ROC curves demonstrate that the SML algorithm achieves a superior performance when compared with the other algorithms for HSI subpixel target detection. The other important evaluation index for target detection is the FAR at TRR = 100%, which is plotted in Fig. 7(b). These results

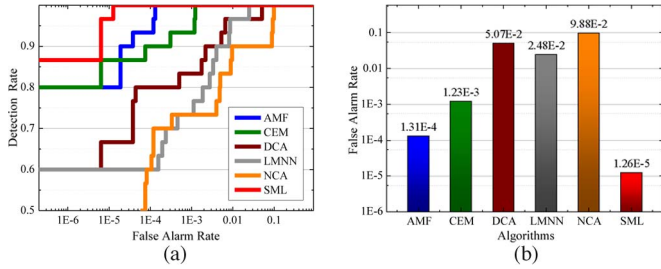


Fig. 7. (a) ROC curves and (b) FAR under 100% detection in the linear implanted target experiment.

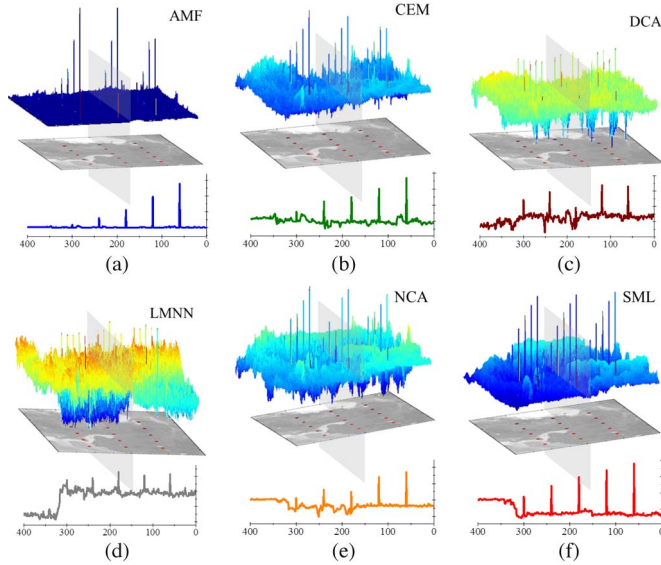


Fig. 8. Three-dimensional target detection test statistic plots and 1-D transect plots of (a) AMF, (b) CEM, (c) DCA, (d) LMNN, (e) NCA, and (f) SML in the nonlinear implanted target experiment.

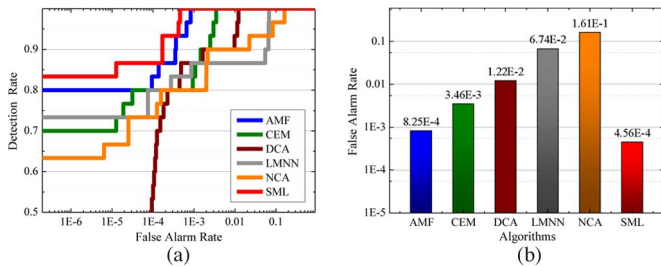


Fig. 9. (a) ROC curves and (b) FAR under 100% detection in the nonlinear implanted target experiment.

also suggest that the proposed SML algorithm results in the lowest FAR when all the target pixels have been recognized.

2) *Nonlinear Implanted Target Detection Results:* The HSI target recognition results in the nonlinear implanted target experiment are similar to the linear condition. The 3-D target detection test statistic plots and the 1-D target detection test statistic transect plots of sample 200 are shown in Fig. 8(a)–(f), respectively. These test statistic plots indicate the outstanding target–background separability of the proposed SML when compared with the other methods. Based on the test statistic plots in Fig. 8(a)–(f), the target detection ROC curves of all the algorithms are shown in Fig. 9(a), in which the curve of SML is clearly in the upper-left location in the figure. In this curve,

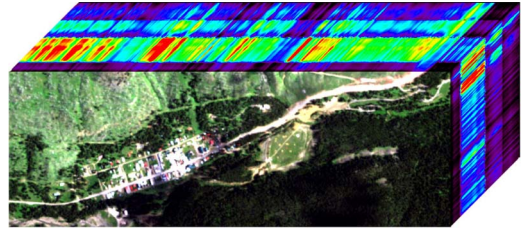


Fig. 10. HyMap data cube of the RIT project.

the FAR is reduced to the 10⁻⁴ level when the TRR is at 90%. According to the experimental results reported here, both the linear and nonlinear implanted target experiments suggest that the proposed SML is an effective approach for HSI subpixel target detection.

B. HyMap Experiment

Fig. 10 shows the HyMap data cube of the RIT project. In this data project, since both the radiance and the scaled reflectance version of the HSI are available, we use the scaled reflectance image and rescale the whole image by a reflectance factor of 10000 to the standard reflectance image. This HSI scene is airborne data, and the sensor was flown at approximately 1.4 km above the terrain, yielding a 3-m ground spatial resolution. Thus, the main background land cover classes can be manually interpreted, and comprise roof, road, soil, grass, tree, and shadow, as shown in Fig. 10.

In this hyperspectral target detection image, several fabric panels and vehicles of various sizes are deployed as targets. Details of these targets are listed in Table II. As the project provides the target size, we can infer that fabrics F1 and F2 (3 m × 3 m) are nearly a full pixel, whereas all the other fabric targets are smaller than a pixel and therefore occupy subpixels in the HyMap image. As regards the three vehicle targets, they occupy, at most, one or two pixels, which will also appear as subpixels in the HSI, as shown in Table II. In summary, all the subpixel targets in the HSI are visually difficult to recognize, and the only information we can use comes from the discriminative information brought about by the spectral signature.

The prior spectrum of each target is obtained and preprocessed by the project-equipped SPL files. The SPL spectra were collected in the field using an Analytical Spectral Device, i.e., a FieldSpec Pro field spectrometer (note that the SPL were not measured in the air by the HyMap sensor), which can measure the reflectance spectra from 350 to 2500 nm, with approximately 1-nm spectral resolution. Then, by rescaling the SPL spectra to the true reflectance data (according to its reflectance factor of 100) and resampling the SPL spectra according to the HSI wavelength, we obtain the prior target spectra for the HSI target detection, as given in Fig. 11(a) and (b). For the distance metric learning algorithms, we manually select ten negative samples that represent the different background land cover classes in the HyMap image. The negative samples are shown in Fig. 12(a), and their spectral curves are shown in Fig. 12(b). We then generate the positive samples by the same approach used for the AVIRIS data set.

TABLE II
LIST OF THE TARGETS IN THE HYMAP SELF-TEST DATA SET


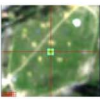

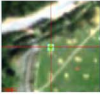
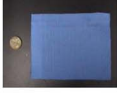









Index	Description and coordinates	Photo	Location in the HSI
F1	Red cotton 3 m × 3 m (138, 504)		
F2	Yellow nylon 3 m × 3 m (122, 484)		
F3 a & b	Blue cotton 2 m × 2 m, (122, 494) 1 m × 1 m, (127, 490)		
F4 a & b	Red nylon 2 m × 2 m, (144, 516) 1 m × 1 m, (152, 514)		
V1	Green Chevy Blazer (128, 339)		
V2	White Toyota T100 (156, 353)		
V3	Red Subaru GL (186, 282)		

TABLE III
TARGET DETECTION FARs FOR THE HYMAP DATA SET

	AMF	CEM	DCA	LMNN	NCA	SML
F1	5.00×10^{-4}	7.68×10^{-4}	8.64×10^{-3}	1.99×10^{-2}	2.35×10^{-3}	1.86×10^{-4}
F2	4.46×10^{-4}	5.22×10^{-4}	2.73×10^{-3}	1.41×10^{-3}	4.08×10^{-3}	3.61×10^{-4}
F3a	1.24×10^{-2}	4.93×10^{-3}	5.61×10^{-3}	1.77×10^{-2}	2.56×10^{-2}	1.32×10^{-3}
F3b	8.82×10^{-2}	4.38×10^{-2}	2.93×10^{-2}	2.79×10^{-2}	6.90×10^{-2}	4.09×10^{-3}
F4a	4.24×10^{-4}	4.15×10^{-4}	4.24×10^{-3}	3.50×10^{-3}	1.50×10^{-2}	1.02×10^{-4}
F4b	8.88×10^{-3}	1.94×10^{-2}	3.37×10^{-2}	3.79×10^{-2}	2.34×10^{-2}	7.36×10^{-3}
V1	1.57×10^{-2}	1.21×10^{-2}	5.56×10^{-3}	2.75×10^{-3}	9.09×10^{-3}	1.62×10^{-3}
V2	1.09×10^{-2}	7.62×10^{-3}	7.92×10^{-3}	3.84×10^{-3}	9.69×10^{-3}	1.04×10^{-3}
V3	1.37×10^{-1}	1.22×10^{-1}	3.76×10^{-2}	5.81×10^{-2}	7.45×10^{-2}	2.01×10^{-2}

TABLE IV
PARAMETER SETTINGS OF THE SML ALGORITHM IN TABLE III

	F1	F2	F3a	F3b	F4a	F4b	V1	V2	V3
t	4.23×10^{-1}	1.67×10^{-2}	6.69×10^{-1}	6.69×10^{-1}	1.85×10^{-1}	1.85×10^{-1}	2.67×10^{-1}	4.17×10^{-1}	4.75×10^{-1}
β	10^{-3}	10^{-3}	10^{-2}	10^{-2}	10^{-3}	10^{-3}	10^{-5}	10^{-3}	10^{-2}
μ	10^{-4}	10^{-3}	10^{-5}	10^{-5}	10^{-4}	10^{-4}	10^{-5}	10^{-4}	10^{-6}

target detection FARs of the six algorithms in Table III. The FAR is defined as the number of pixels that have a test statistic value equal to or lower than the target pixel value, divided by the total number of pixels in the HSI (i.e., 224 000 in the HSI we analyzed). It is evident from Table III that the proposed SML algorithm gives a superior performance for all the targets in the HyMap experiment.

V. CONCLUSION

In order to deal with the challenge of hyperspectral remote sensing image subpixel target detection, we have proposed a novel SML algorithm, which is based on a machine learning perspective. The SML algorithm learns a distance metric for the hyperspectral target detection that leads to effective target–background separability by the optimization of three parts: 1) a supervised distance maximization, which maximizes the average distance between the positive and negative samples; 2) a similarity propagation constraint, which simultaneously links target pixels with positive samples, as well as the background pixels with negative samples, which helps to reject the false alarms in target detection; and 3) a manifold smoothness regularization, which preserves the local geometry of the positive samples in the obtained metric. Furthermore, the solution of SML can be simply obtained by implementing the standard eigenvalue decomposition command. Experiments with HSI subpixel target detection using public data sets confirm the superior performance of our algorithm. Compared with the effective HSI subpixel target detection algorithms AMF and CEM, as well as some other well-known distance metric learning methods, in mineral detection in an AVIRIS image and fabric and vehicle detection in a HyMap image, our SML algorithm achieves the best results in the target–background separability analysis, ROC curve statistics, and FAR evaluation.

ACKNOWLEDGMENT

The authors would like to thank the anonymous reviewers for their insightful and constructive comments. The authors would also like to thank the researchers from the RIT for providing the hyperspectral target detection data set.

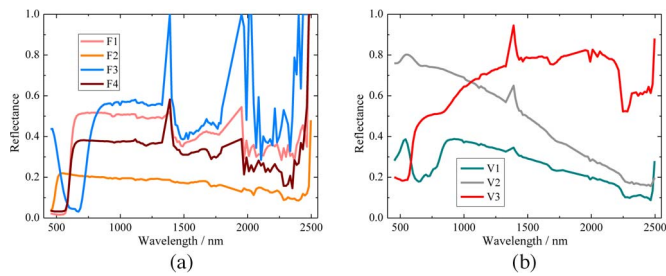


Fig. 11. Prior spectral signatures of all the desired targets after preprocessing. (a) Fabrics F1–F4. (b) Vehicles V1–V3.

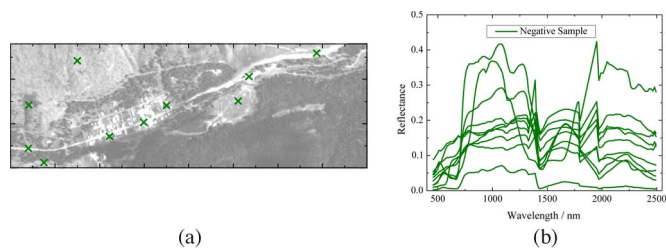


Fig. 12. Selected negative (a) sample locations and (b) spectra for the metric learning algorithms in the HyMap data set.

The HyMap image target detection results for all the methods are listed in Table III, and the detailed parameter settings are provided in Table IV. Since it is a real-world HSI scene and there is a unique true location for each target, we compare the

REFERENCES

- [1] A. F. H. Goetz, G. Vane, J. E. Solomon, and B. N. Rock, "Imaging spectrometry for Earth remote sensing," *Science*, vol. 228, no. 4704, pp. 1147–1153, Jun. 1985.
- [2] R. O. Green, M. L. Eastwood, C. M. Sarture, T. G. Chrien, M. Aronsson, B. J. Chippendale, J. A. Faust, B. E. Pavri, C. J. Chovit, M. Solis, M. R. Olah, and O. Williams, "Imaging spectroscopy and the Airborne Visible/Infrared Imaging Spectrometer (AVIRIS)," *Remote Sens. Environ.*, vol. 65, no. 3, pp. 227–248, Sep. 1998.
- [3] T. Cocks, R. Janssen, A. Stewart, I. Wilson, and T. Shields, "The HyMap™ airborne hyperspectral sensor: The system, calibration and performance," in *Proc. EARSEL Workshop Imag. Spectrosc.*, 1998, pp. 37–42.
- [4] D. Manolakis, D. Marden, and G. A. Shaw, "Hyperspectral image processing for automatic target detection applications," *Lincoln Lab. J.*, vol. 14, no. 1, pp. 79–116, Jan. 2003.
- [5] J. P. Kerekes and J. E. Baum, "Spectral imaging system analytical model for subpixel object detection," *IEEE Trans. Geosci. Remote Sens.*, vol. 40, no. 5, pp. 1088–1101, May 2002.
- [6] B. Du and L. Zhang, "Random-selection-based anomaly detector for hyperspectral imagery," *IEEE Trans. Geosci. Remote Sens.*, vol. 49, no. 5, pp. 1578–1589, May 2011.
- [7] J. J. Settle and N. A. Drake, "Linear mixing and the estimation of ground cover proportions," *Int. J. Remote Sens.*, vol. 14, no. 6, pp. 1159–1177, 1993.
- [8] A. Plaza, Q. Du, J. M. Bioucas-Dias, X. Jia, and F. A. Kruse, "Foreword to the special issue on spectral unmixing of remotely sensed data," *IEEE Trans. Geosci. Remote Sens.*, vol. 49, no. 11, pp. 4103–4110, Nov. 2011.
- [9] N. Keshava and J. F. Mustard, "Spectral unmixing," *IEEE Signal Process. Mag.*, vol. 19, no. 1, pp. 44–57, Jan. 2002.
- [10] J. M. Bioucas-Dias, A. Plaza, N. Dobigeon, M. Parente, Q. Du, P. Gader, and J. Chanussot, "Hyperspectral unmixing overview: Geometrical, statistical, and sparse regression-based approaches," *IEEE J. Sel. Topics Appl. Earth Observ. Remote Sens.*, vol. 5, no. 2, pp. 354–379, Apr. 2012.
- [11] S. Matteoli, N. Acito, M. Diani, and G. Corsini, "An automatic approach to adaptive local background estimation and suppression in hyperspectral target detection," *IEEE Trans. Geosci. Remote Sens.*, vol. 49, no. 2, pp. 790–800, Feb. 2011.
- [12] D. Manolakis, C. Siracusa, and G. Shaw, "Hyperspectral subpixel target detection using the linear mixing model," *IEEE Trans. Geosci. Remote Sens.*, vol. 39, no. 7, pp. 1392–1409, Jul. 2001.
- [13] Q. Du and C.-I. Chang, "A signal-decomposed and interference-annihilated approach to hyperspectral target detection," *IEEE Trans. Geosci. Remote Sens.*, vol. 42, no. 4, pp. 892–906, Apr. 2004.
- [14] I. S. Reed, J. D. Mallett, and L. E. Brennan, "Rapid convergence rate in adaptive arrays," *IEEE Trans. Aerosp. Electron. Syst.*, vol. AES-10, no. 6, pp. 853–863, Nov. 1974.
- [15] F. C. Robey, D. R. Fuhrmann, E. J. Kelly, and R. Nitzberg, "A CFAR adaptive matched filter detector," *IEEE Trans. Aerosp. Electron. Syst.*, vol. 28, no. 1, pp. 208–216, Jan. 1992.
- [16] S. Kraut and L. L. Scharf, "The CFAR adaptive subspace detector is a scale-invariant GLRT," *IEEE Trans. Signal Process.*, vol. 47, no. 9, pp. 2538–2541, Sep. 1999.
- [17] S. Kraut, L. L. Scharf, and L. T. McWhorter, "Adaptive subspace detectors," *IEEE Trans. Signal Process.*, vol. 49, no. 1, pp. 1–16, Jan. 2001.
- [18] L. Zhang, B. Du, and Y. Zhong, "Hybrid detectors based on selective endmembers," *IEEE Trans. Geosci. Remote Sens.*, vol. 48, no. 6, pp. 2633–2646, Jun. 2010.
- [19] J. Broadwater and R. Chellappa, "Hybrid detectors for subpixel targets," *IEEE Trans. Pattern Anal. Mach. Intell.*, vol. 29, no. 11, pp. 1891–1903, Nov. 2007.
- [20] L. Zhang, L. Zhang, D. Tao, and X. Huang, "On combining multiple features for hyperspectral remote sensing image classification," *IEEE Trans. Geosci. Remote Sens.*, vol. 50, no. 3, pp. 879–893, Mar. 2012.
- [21] W. Li, S. Prasad, J. E. Fowler, and L. M. Bruce, "Locality-preserving dimensionality reduction and classification for hyperspectral image analysis," *IEEE Trans. Geosci. Remote Sens.*, vol. 50, no. 4, pp. 1185–1198, Apr. 2012.
- [22] J. Li, J. M. Bioucas-Dias, and A. Plaza, "Semisupervised hyperspectral image segmentation using multinomial logistic regression with active learning," *IEEE Trans. Geosci. Remote Sens.*, vol. 48, no. 11, pp. 4085–4098, Nov. 2010.
- [23] G. Bilgin, S. Ertrk, and T. Yldrm, "Segmentation of hyperspectral images via subtractive clustering and cluster validation using one-class support vector machines," *IEEE Trans. Geosci. Remote Sens.*, vol. 49, no. 8, pp. 2936–2944, Aug. 2011.
- [24] M. Fauvel, J. A. Benediktsson, J. Chanussot, and J. R. Sveinsson, "Spectral and spatial classification of hyperspectral data using SVMs and morphological profiles," *IEEE Trans. Geosci. Remote Sens.*, vol. 46, no. 11, pp. 3804–3814, Nov. 2008.
- [25] L. Bruzzone, M. Chi, and M. Marconcini, "A novel transductive SVM for semisupervised classification of remote-sensing images," *IEEE Trans. Geosci. Remote Sens.*, vol. 44, no. 11, pp. 3363–3373, Nov. 2006.
- [26] L. Zhang, L. Zhang, D. Tao, and X. Huang, "Sparse transfer manifold embedding for hyperspectral target detection," *IEEE Trans. Geosci. Remote Sens.*, vol. 52, no. 3, Mar. 2014. [Online]. Available: <http://ieeexplore.ieee.org>
- [27] H. Kwon and N. M. Nasrabadi, "Kernel spectral matched filter for hyperspectral imagery," *Int. J. Comput. Vis.*, vol. 71, no. 2, pp. 127–141, Feb. 2007.
- [28] L. Capobianco, A. Garzelli, and G. Camps-Valls, "Target detection with semisupervised kernel orthogonal subspace projection," *IEEE Trans. Geosci. Remote Sens.*, vol. 47, no. 11, pp. 3822–3833, Nov. 2009.
- [29] Y. Chen, N. M. Nasrabadi, and T. D. Tran, "Simultaneous joint sparsity model for target detection in hyperspectral imagery," *IEEE Geosci. Remote Sens. Lett.*, vol. 8, no. 4, pp. 676–680, Jul. 2011.
- [30] Y. Chen, N. M. Nasrabadi, and T. D. Tran, "Sparse representation for target detection in hyperspectral imagery," *IEEE J. Sel. Top. Signal Process.*, vol. 5, no. 3, pp. 629–640, Jun. 2011.
- [31] E. P. Xing, A. Y. Ng, M. I. Jordan, and S. Russell, "Distance metric learning, with application to clustering with side-information," in *Proc. NIPS*, 2002, pp. 505–512.
- [32] J. Goldberger, S. Roweis, G. Hinton, and R. Salakhutdinov, "Neighbourhood components analysis," in *Proc. NIPS*, 2004, pp. 513–520.
- [33] K. Q. Weinberger and L. K. Saul, "Distance metric learning for large margin nearest neighbor classification," *J. Mach. Learn. Res.*, vol. 10, pp. 207–244, Jun. 2009.
- [34] S. C. H. Hoi, W. Liu, M. R. Lyu, and W.-Y. Ma, "Learning distance metrics with contextual constraints for image retrieval," in *Proc. CVPR*, 2006, pp. 2072–2078.
- [35] Z. Hong, X. Mei, and D. Tao, "Dual-force metric learning for robust distracter-resistant tracker," in *Proc. ECCV*, 2012, pp. 513–527.
- [36] C.-C. Chang, "A boosting approach for supervised Mahalanobis distance metric learning," *Pattern Recogn.*, vol. 45, no. 2, pp. 844–862, Feb. 2012.
- [37] D. Manolakis and G. Shaw, "Detection algorithms for hyperspectral imaging applications," *IEEE Signal Process. Mag.*, vol. 19, no. 1, pp. 29–43, Jan. 2002.
- [38] F. Wang, "Semisupervised metric learning by maximizing constraint margin," *IEEE Trans. Syst. Man Cybern. Part B, Cybern.*, vol. 41, no. 4, pp. 931–939, Aug. 2011.
- [39] J. Yu, M. Wang, and D. Tao, "Semi-supervised multiview distance metric learning for cartoon synthesis," *IEEE Trans. Image Process.*, vol. 21, no. 11, pp. 4636–4648, Nov. 2012.
- [40] J. V. Davis, B. Kulis, P. Jain, S. Sra, and I. S. Dhillon, "Information-theoretic metric learning," in *Proc. ICML*, 2007, pp. 209–216.
- [41] N. Sental, T. Hertz, D. Weinshall, and M. Pavel, "Adjustment learning and relevant component analysis," in *Proc. ECCV*, 2002, pp. 776–790.
- [42] D. Tao, X. Tang, X. Li, and Y. Rui, "Direct kernel biased discriminant analysis: A new content-based image retrieval relevance feedback algorithm," *IEEE Trans. Multimedia*, vol. 8, no. 4, pp. 716–727, Aug. 2006.
- [43] M. Belkin and P. Niyogi, "Laplacian eigenmaps for dimensionality reduction and data representation," *Neural Comput.*, vol. 15, no. 6, pp. 1373–1396, Mar. 2003.
- [44] W. Liu, X. Tian, D. Tao, and J. Liu, "Constrained metric learning via distance gap maximization," in *Proc. AAAI*, 2010, pp. 518–524.
- [45] D. Zhou, O. Bousquet, T. N. Lal, J. Weston, and B. Scholkopf, "Learning with local and global consistency," in *Proc. NIPS*, 2004, pp. 321–328.
- [46] J. Kandola, J. Shawe-Taylor, and N. Cristianini, "Learning semantic similarity," in *Proc. NIPS*, 2002, pp. 657–664.
- [47] T. Zhou and D. Tao, "Double shrinking for sparse dimension reduction," *IEEE Trans. Image Process.*, vol. 22, no. 1, pp. 244–257, Jan. 2013.
- [48] W. Liu and D. Tao, "Multiview Hessian regularization for image annotation," *IEEE Trans. Image Process.*, vol. 22, no. 7, pp. 2676–2687, Jul. 2013.
- [49] S. T. Roweis and L. K. Saul, "Nonlinear dimensionality reduction by locally linear embedding," *Science*, vol. 290, no. 22, pp. 2323–2326, Dec. 2000.
- [50] S. Yan, D. Xu, B. Zhang, H.-J. Zhang, Q. Yang, and S. Lin, "Graph embedding and extensions: A general framework for dimensionality reduction," *IEEE Trans. Pattern Anal. Mach. Intell.*, vol. 29, no. 1, pp. 40–51, Jan. 2007.
- [51] T. Zhang, D. Tao, X. Li, and J. Yang, "Patch alignment for dimensionality reduction," *IEEE Trans. Knowl. Data Eng.*, vol. 21, no. 9, pp. 1299–1313, Sep. 2009.

- [52] C.-I. Chang and D. C. Heinz, "Constrained subpixel target detection for remotely sensed imagery," *IEEE Trans. Geosci. Remote Sens.*, vol. 38, no. 3, pp. 1144–1159, Aug. 2000.
- [53] J. C. Harsanyi and C.-I. Chang, "Hyperspectral image classification and dimensionality reduction: An orthogonal subspace projection approach," *IEEE Trans. Geosci. Remote Sens.*, vol. 32, no. 4, pp. 779–785, Jul. 1994.
- [54] D. Snyder, J. Kerekes, I. Fairweather, R. Crabtree, J. Shive, and S. Hager, "Development of a web-based application to evaluate target finding algorithms," in *Proc. IGARSS*, 2008, pp. 915–918.
- [55] J. Kerekes, "Receiver operating characteristic curve confidence intervals and regions," *IEEE Geosci. Remote Sens. Lett.*, vol. 5, no. 2, pp. 251–255, Apr. 2008.



Lefei Zhang (S'11–M'14) received the B.S. degree in sciences and techniques of remote sensing and the Ph.D. degree in photogrammetry and remote sensing from Wuhan University, Wuhan, China, in 2008 and 2013, respectively.

In August 2013, he joined the Computer School, Wuhan University, where he is currently an Assistant Professor. His research interests include hyperspectral data analysis, high-resolution image processing, and pattern recognition in remote sensing images.

Dr. Zhang is a Reviewer of more than ten international journals, including the *IEEE TRANSACTIONS ON GEOSCIENCE AND REMOTE SENSING*, the *IEEE JOURNAL OF SELECTED TOPICS IN APPLIED EARTH OBSERVATIONS AND REMOTE SENSING*, the *IEEE GEOSCIENCE AND REMOTE SENSING LETTERS*, *Information Sciences*, and *Pattern Recognition*.

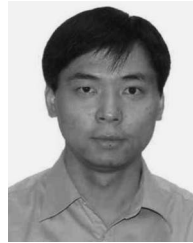


Liangpei Zhang (M'06–SM'08) received the B.S. degree in physics from Hunan Normal University, Changsha, China, in 1982, the M.S. degree in optics from the Chinese Academy of Sciences, Xian, China, in 1988, and the Ph.D. degree in photogrammetry and remote sensing from Wuhan University, Wuhan, China, in 1998.

He is currently the Head of the Remote Sensing Division, State Key Laboratory of Information Engineering in Surveying, Mapping and Remote Sensing, Wuhan University. He is also a Chang-Jiang Scholar

Chair Professor appointed by the Ministry of Education of China. He is currently a Principal Scientist for the China State Key Basic Research Project (2011–2016) appointed by the Ministry of National Science and Technology of China to lead the remote sensing program in China. He has more than 300 research papers. He is the holder of five patents. His research interests include hyperspectral remote sensing, high-resolution remote sensing, image processing, and artificial intelligence.

Dr. Zhang is a Fellow of the The Institution of Engineering and Technology, an Executive Member (Board of Governor) of the China National Committee of the International Geosphere-Biosphere Programme, and an Executive Member of the China Society of Image and Graphics. He regularly serves as a Cochair of the series SPIE Conferences on Multispectral Image Processing and Pattern Recognition, Conference on Asia Remote Sensing, and many other conferences. He edits several conference proceedings, issues, and geoinformatics symposiums. He also serves as an Associate Editor of the *International Journal of Ambient Computing and Intelligence*, the *International Journal of Image and Graphics*, the *International Journal of Digital Multimedia Broadcasting*, the *Journal of Geo-spatial Information Science*, the *Journal of Remote Sensing*, and the *IEEE TRANSACTIONS ON GEOSCIENCE AND REMOTE SENSING*.



Dacheng Tao (M'07–SM'12) received the B.Eng. degree from the University of Science and Technology of China, Hefei, China, the M.Phil. degree from The Chinese University of Hong Kong, Hong Kong, and the Ph.D. degree from the University of London, London, U.K.

He is a Professor of computer science with the Centre for Quantum Computation and Information Systems and the Faculty of Engineering and Information Technology, University of Technology, Sydney, Ultimo, NSW, Australia. He mainly applies

statistics and mathematics for data analysis problems in data mining, computer vision, machine learning, multimedia, and video surveillance. He has authored and coauthored more than 100 scientific articles at top venues, including the *IEEE TRANSACTIONS ON PATTERN ANALYSIS AND MACHINE INTELLIGENCE*, *IEEE TRANSACTIONS ON KNOWLEDGE AND DATA ENGINEERING*, *IEEE TRANSACTIONS ON IMAGE PROCESSING*, *Neural Information Processing Systems*, International Conference on Machine Learning, The Conference on Uncertainty in Artificial Intelligence, International Conference on Artificial Intelligence and Statistics, International Conference on Data Mining (ICDM), International Joint Conference on Artificial Intelligence, Association for the Advancement of Artificial Intelligence, IEEE International Conference on Computer Vision and Pattern Recognition, European Conference on Computer Vision, *ACM Transactions on Knowledge Discovery from Data*, *Multimedia*, and International Conference on Knowledge Discovery and Data Mining.

Prof. Tao was the recipient of the Best Theory/Algorithm Paper runner up award in IEEE ICDM07.



Xin Huang (M'13) received the Ph.D. degree in photogrammetry and remote sensing from Wuhan University, Wuhan, China, in 2009.

He is currently a Full Professor with the State Key Laboratory for Information Engineering in Surveying, Mapping and Remote Sensing, Wuhan University. He has published more than 35 peer-reviewed articles in international journals. He has frequently served as a referee for many international journals for remote sensing. His research interests include hyperspectral data analysis, high-resolution image processing, pattern recognition, and remote sensing applications.

Dr. Huang was the recipient of the Top Ten Academic Star of Wuhan University in 2009, the Boeing Award for the best paper in image analysis and interpretation from the American Society for Photogrammetry and Remote Sensing in 2010, the New Century Excellent Talents in University from the Ministry of Education of China in 2011, and the National Excellent Doctoral Dissertation Award of China in 2012. In 2011, he was recognized by the IEEE Geoscience and Remote Sensing Society as the Best Reviewer of the *IEEE GEOSCIENCE AND REMOTE SENSING LETTERS*.



Bo Du (M'12) received the B.S. degree and the Ph.D. degree in photogrammetry and remote sensing from Wuhan University, Wuhan, China, in 2005 and 2010, respectively.

He is currently an Associate Professor with the Computer School, Wuhan University. His major research interests include pattern recognition, hyperspectral image processing, and signal processing.